Predicting spatial patterns of coseismic shallow landslides: the critical role of regolith thickness in earthquake-prone terrain

Ghoshal, Suryodoy*,[1], Boulton, Sarah J.[1], Hales, Tristram C.[2], Bennett, Georgie E.[3], Beswick, Amy[1], Jones, Joshua N.[4], Lewin, Shaun[1], Mildon, Zoë K.[1], Stokes, Martin[1], Whitworth, Michael R. Z.[4], Campforts, Benjamin[5]

[1] Centre for Research in Natural Hazards and Risk Reduction, University of Plymouth, Plymouth, United Kingdom
[2] School of Earth and Environmental Sciences, Cardiff University, Cardiff, United Kingdom
[3] Department of Geography, University of Exeter, Exeter, United Kingdom
[4] AECOM, Ground Engineering, Plymouth, United Kingdom
[5] Department of Earth Sciences, Vrije Universiteit Amsterdam, Amsterdam, The Netherlands

Key Points

- Landscape-scale patterns of coseismic shallow landsliding are controlled primarily by regolith-thickness organisation.
- Model reproduces mapped Gorkha landslide distributions best with moderate effective cohesion of between 10 to 15 kPa.
- High relief terrain shows elevation-driven regolith thinning; soil-mantled hillslopes show curvature-driven convergence.

Keywords

coseismic landslides; regolith thickness; slope stability; Himalayan hazards; Newmark method

---

* suryodoy.ghoshal@plymouth.ac.uk

Abstract

Earthquake-triggered landslides are a dominant agent of sediment mobilisation in steep terrain, yet the physical controls that organise coseismic shallow-failure patterns across landscapes remain incompletely understood. In particular, the influence of regolith thickness and its spatial organisation on regional-scale failure patterns has been difficult to quantify. Here we introduce *ShallowLandslider*, a hybrid physical-statistical framework that couples a three-dimensional Newmark stability formulation with topographically informed regolith-thickness fields and population-level realisation of landslide patches. We evaluate the model in two geomorphically distinct subregions impacted by the 2015 Gorkha earthquake, assessing its ability to reproduce observed patterns of landslide occurrence and area across elevation, slope and aspect.

Across all configurations, the spatial structure of regolith thickness exerts the strongest control on the distribution of coseismic shallow landsliding. Parameterisations incorporating realistic regolith-thickness variability consistently outperform a uniform-depth baseline, and model performance peaks at moderate cohesion values ($c' \approx 10$–$15\,\mathrm{kPa}$) characteristic of shallow colluvium. The two subregions exhibit contrasting dominant controls: in the high-relief, bedrock-dominated terrain of Subregion 1, landslide patterns are best simulated when regolith organisation is represented by broad hypsometric thinning, whereas in the lower-relief, regolith-mantled terrain of Subregion 2, curvature-informed parameterisations capturing local hillslope convergence provide the closest agreement with the mapped landslide population. Our findings demonstrate that a process-based model respecting the physics controlling shallow landsliding performs reliably only when the spatial variability of regolith thickness is accurately represented. This indicates that landscape-scale patterns of regolith thickness, not uncertainty in failure mechanics, explain regional variation in landslide response.

Plain Language Summary

Large earthquakes can trigger thousands of landslides that move soil (regolith) from hillslopes into rivers, threatening people and infrastructure. Predicting where these landslides happen is challenging because near-surface materials vary across landscapes. We present ShallowLandslider, a model that combines simplified physics of slope stability with realistic maps of regolith thickness to predict patterns of shallow landsliding. We test the model in two parts of Nepal affected by the 2015 Gorkha earthquake and compare predictions to a detailed inventory of observed landslides. We find that how regolith thickness is organized across the landscape is the single most important factor controlling landslide patterns. In very rugged, bedrock-dominated terrain, landslides concentrate where regolith thins systematically with elevation. In gentler, soil-mantled terrain, landslides cluster in convergent hollows where regolith accumulates. The best agreement with observations occurs for moderate cohesion values typical of loose colluvium, supporting the conclusion that most Gorkha landslides were shallow, regolith-sourced. Our results show that large-scale predictions of coseismic landslides depend less on uncertain failure mechanics and more on the landscape-scale distribution of regolith thickness, pointing to new priorities

for mapping and monitoring in earthquake-prone mountains.

1 Introduction

Major earthquakes commonly trigger thousands of landslides across mountainous terrain, (re)mobilising regolith and rock over spatial extents of tens to hundreds of square kilometres. Coseismic landslides constitute a major secondary hazard, frequently disrupting infrastructure, damming rivers, and causing loss of life and economic damage that can sometimes rival the initial impacts of the earthquake itself (Fan et al., 2019; Petley, 2012). Beyond their immediate societal consequences, coseismic landslides exert a first-order control on mountain evolution by rapidly transferring sediment from hillslopes to channels, perturbing drainage networks, and influencing post-seismic erosion patterns (Campforts et al., 2022; Hovius et al., 2011; Wang et al., 2020). Understanding the physical controls on where coseismic landslides occur, and how their spatial characteristics vary across landscapes, is therefore central to both regional hazard assessment and the feedbacks between tectonics, climate, and surface processes.

Despite decades of research, the physical controls that organise the spatial structure of coseismic landslide populations remain difficult to quantify. Empirical and statistical susceptibility models use observed spatial relationships between landslide occurrence and terrain parameters such as slope angle, aspect, lithology, and distance to faults (e.g., Kritikos et al., 2015; Parker et al., 2015). While these empirical/statistical approaches are computationally efficient and perform well when trained on high-quality landslide inventories, they are inherently event-specific, reflecting the characteristics of the earthquake and terrain from which they were derived. As a result, the transferability to new regions or earthquakes with different ground motion patterns can be limited (Gariano and Guzzetti, 2016; Tanyaş et al., 2017). Emerging machine-learning approaches can capture more complex relationships, but, like traditional susceptibility models, they offer limited physical interpretability and depend heavily on the quality of training data (Lombardo et al., 2020; Nowicki Jessee et al., 2018; Reichenbach et al., 2018). However, empirical susceptibility models retain important advantages; because they treat landsliding as a stochastic outcome of multiple conditioning factors, they naturally accommodate the intrinsic variability of parameters such as regolith properties, hydrologic conditions, and local roughness, features that are difficult to specify deterministically in regional models. In contrast, physics-based models explicitly represent the mechanical processes governing slope failure and are therefore better suited for local hypothesis testing and extrapolation across diverse geomorphic and seismic settings. Among these, the Newmark sliding block method remains the most widely used for assessing coseismic slope stability. The method conceptualizes a potential landslide as a rigid block resting on an inclined plane, which begins to slide once the driving acceleration exceeds a critical threshold determined by slope geometry and material strength (Jibson et al., 2000; Jibson, 2007; Newmark, 1965; Romeo, 2000). Its simplicity and robustness enable regional-scale implementation, particularly when combined with digital elevation models (DEMs) and spatially distributed ground-motion data. As such, it has been widely applied to simulate coseismic landslides, particularly where shallow failures dominate the landscape response. However, deterministic physics-based (e.g., Newmark) applications remain highly sensitive to material properties, like regolith thickness, effective cohesion, and friction angle, whose spatial variability is rarely constrained and difficult to measure directly at landscape scales (Huang et al., 2020; Segoni et al., 2012). A further complication is that traditional Newmark applications were developed primarily for deep-seated or bedrock failures, whereas many large earthquakes, such as the 2015 M_w 7.8 Gorkha earthquake, are dominated by shallow, regolith-sourced landslides (Roback et al., 2018). The distinction matters: shallow failures are highly sensitive to variations in regolith thickness, cohesion, and planform curvature, and may therefore reflect the organisation of near-surface materials more strongly than deeper mechanical structure. Accurately representing the spatial variability of regolith thickness is thus essential for understanding landscape-scale patterns of coseismic failure, yet few models systematically evaluate how different assumptions about regolith distribution translate into population-level landslide characteristics. Hybrid modelling frameworks bridge empirical/statistical and physics-based approaches by treating landsliding as a physically constrained but inherently stochastic process. In rainfall-triggered contexts, models such as SINMAP (Pack et al., 1998) and recent iterations of SHALSTAB (Dietrich et al., 1995) have long combined infinite-slope physics with probabilistic hydrologic forcing. However, equivalent hybrid formulations for coseismic landsliding remain comparatively rare, despite large uncertainties in regolith thickness, strength, and local shaking (Huang et al., 2020; Segoni et al., 2012). This gap motivates approaches that combine mechanistic slope-stability calculations with stochastic components that represent unresolved landscape variability.

The 2015 M_w 7.8 Gorkha earthquake in Nepal provides a compelling natural laboratory for examining these issues. The event ruptured a ~150 km segment of the Main Himalayan thrust between the Gorkha region northwest of Kathmandu to the Ramechhap region in eastern-central Nepal (Avouac et al., 2015; USGS, 2015), producing peak ground accelerations (PGA) locally exceeding $0.6g$, and triggering widespread slope failures across an area of more than 30 000 km^2. Over 25,000 landslides were mapped in its aftermath by a succession of groups around the world (Figure 1), making it one of the most comprehensively documented cases of coseismic landsliding worldwide (Kargel et al., 2015; Meena and Tavakkoli Piralilou, 2019; Roback et al., 2018). The failures were concentrated in areas of high PGA and rugged topography north of the Kathmandu valley, with fewer, smaller events occurring in the southern foothills (Roback et al., 2018). The spatial pattern of landsliding closely followed gradients in shaking intensity and local relief, offering an ideal natural experiment for evaluating model performance in real-world conditions. The vast majority of these landslides were shallow, regolith-sourced failures rather than deep-seated bedrock landslides. This distinction is critical: shallow landslides are sensitive to both the spatial organisation of regolith thickness and to moderate cohesion values typical of mobile regolith (Montgomery and Dietrich, 1994). Cohesion values of $\sim$ 10–15 kPa, characteristic of shallow, mobile regolith (Cho and Lee, 2002; Huang et al., 2020; Wong and Ho, 2000), are consistent with realistic failure behaviour for the Gorkha landscape, and reinforce observational evidence that the event was dominated by shallow failures.

In this study, we use a new hybrid physical-statistical framework, *ShallowLandslider*, to examine how the spatial organisation of regolith thickness and the choice of strength parameters control coseismic landslide populations. The model extends the Newmark method to three-dimensions within the Landlab modelling environment, coupling its deterministic slope-stability calculations with a stochastic component that reflects unresolved heterogeneity in natural landscapes. Applying this framework to two geomorphically distinct subregions affected by the Gorkha earthquake, we systematically test a suite of physically motivated regolith-depth parameterisations and assess agreement between model outputs and the landslide inventory using non-parametric distributional metrics for landslide area, mean elevation, mean slope, and aspect. Our goal is to determine how regolith thickness, its spatial variability (e.g., elevation-driven trends, curvature-driven convergence), and its mechanical properties influence coseismic landsliding in each landscape, and to understand why different parameterisations succeed or fail across contrasting landscapes.

2 Methods

2.1 Study area

We evaluate *ShallowLandslider* in two subregions within the landslide-affected zone (Figures 1, 2). These subregions were selected to isolate the influence of contrasting topography and regolith structure under similar shaking conditions, and together they represent complementary test cases for examining the transferability of regolith-depth parameterisations.

Subregion 1 (northwest of Kathmandu): This area lies immediately east of the earthquake epicentre and experienced some of the strongest shaking (PGA $\approx 0.6g$). Despite this, it produced a moderate number of landslides ($n = 523$; Figure 1). Elevations range from ~ 1500–6000 m (mean≈3800 m), with a relief of 4626 m. Slopes vary almost normally between subhorizontal to ∼68° (mean = 37°). Failures mapped in this subregion were concentrated at the lower end of the regional elevation distribution, with very few failures above 4000 m. Failures are largely concentrated at steeper slopes, with most occurring on slopes $> 35° - 50°$ (Figure 2).

Subregion 2 (northeast of Kathmandu): This region follows the Araniko Highway toward the Nepal-China border and is highly landslide-prone, due to both monsoon rainfall and coseismic shaking. It was affected by both the mainshock and the M_w 7.3 aftershock, with PGA $\approx 0.6g$, triggering over 2300 landslides (Figure 1). The average elevation here is considerably lower than in Subregion 1, ranging from 1000 m–3500 m (mean≈2500 m), with a relief of 2712 m. The slope distribution is similar to Subregion 1, ranging between subhorizontal to $\sim 60°$, but with a lower mean (26°). Landslides occur across the full elevation range but again tend to cluster on slopes steeper than 35°–50° (Figure 2). This area is also heavily modified by human activity, particularly along the Araniko corridor, where extensive road construction, slope cutting, and deforestation contribute to locally unstable slopes and increased regolith disturbance. These two landscapes differ strongly in hypsometry, degree

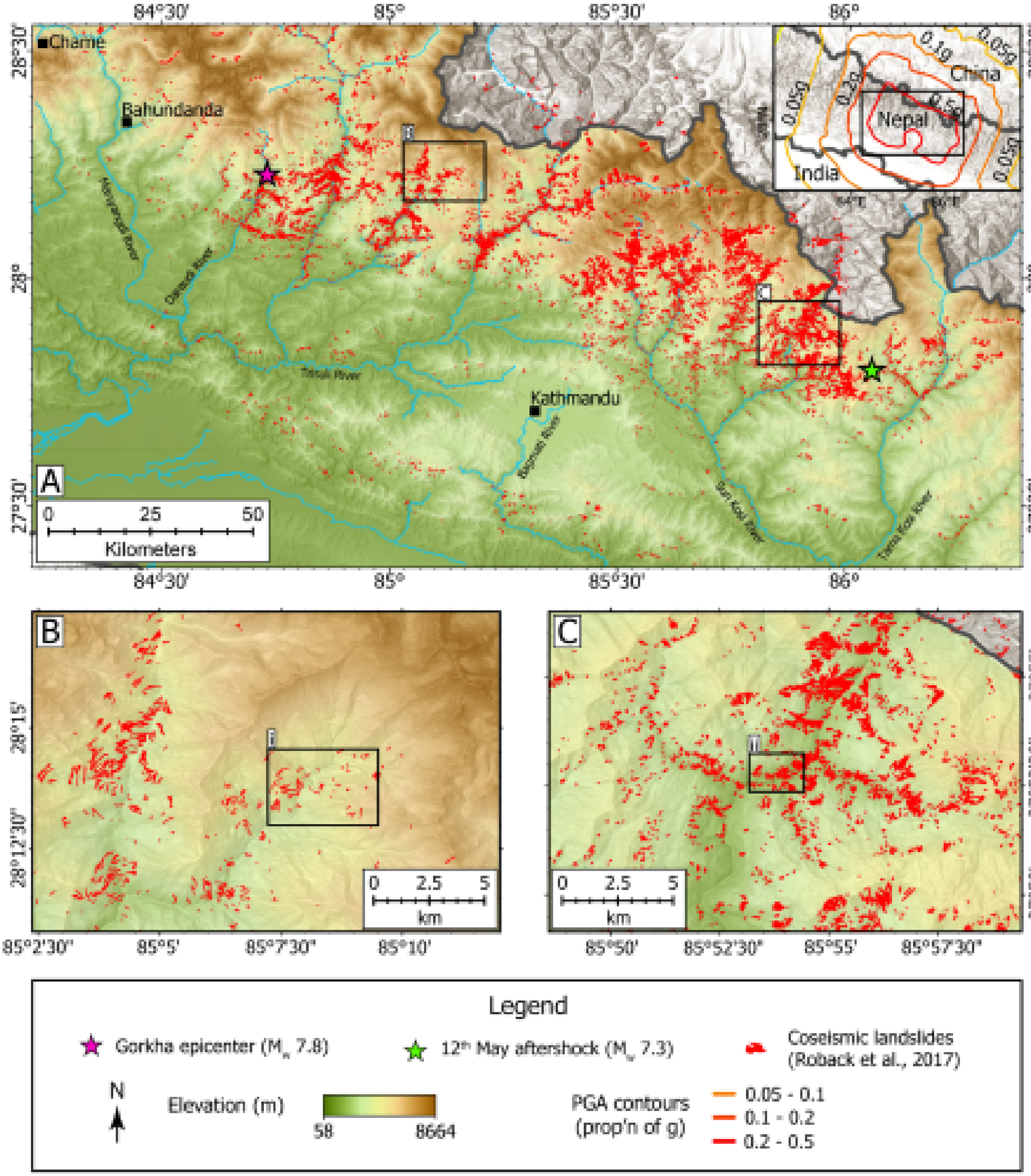

Figure 1: (A) Map of coseismic landslides (red) triggered by the 2015 M_w 7.8 Gorkha earthquake (Roback et al., 2017). The pink star marks the mainshock epicentre and the green star marks the M_w 7.3 aftershock of 12 May 2015. Contours in the inset show peak ground acceleration (proportion of g) from the USGS ShakeMap (USGS, 2015). (B) Topography and mapped landslides in Subregion 1, illustrating its high-relief, bedrock-dominated terrain. (C) Topography and mapped landslides in Subregion 2, which is characterised by lower relief and more extensive regolith mantling. Boxes (i) and (ii) show the locations of the images shown in Figure 2

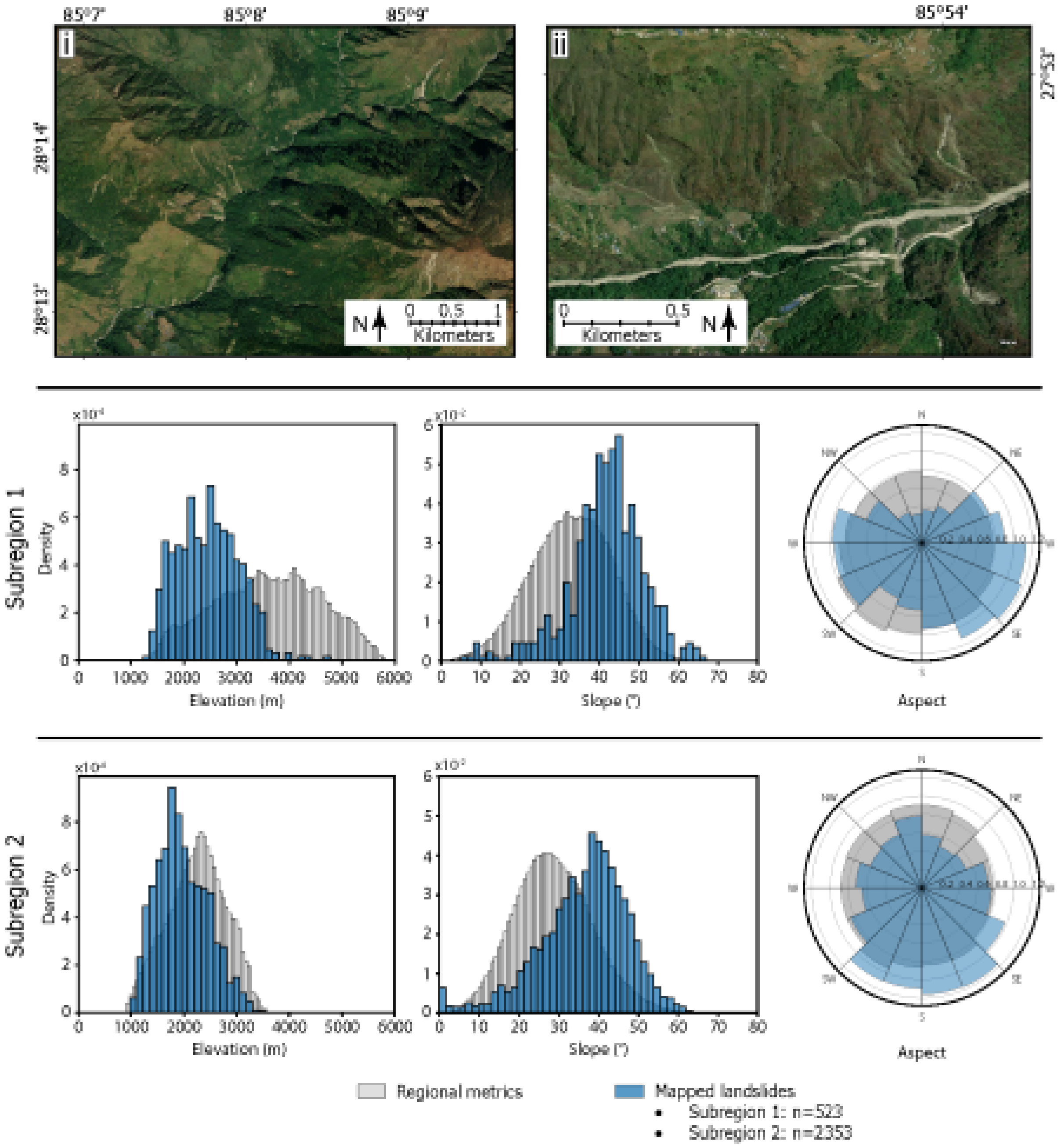

Figure 2: (i) Satellite image of a small part of Subregion 1 showing showing steep, highly dissected, bedrock-dominated topography. (ii) Satellite image of a small part of Subregion 2 showing rolling, regolith-mantled hillslopes with pervasive convergent hollows. Imagery source: Esri, Maxar, Earthstar Geographics, and the GIS User Community (acquired between 2018–2024). Histograms and rose diagrams show the density distributions for elevation and slope in Subregion 1 and Subregion 2. Grey bars show regional distribution, while blue bars show distribution for mapped subregional landslides.

of topographic convergence, and degree of vegetation cover, which reflects differences in the thickness of the soil mantle. This provides a natural test-bed for testing whether broad elevation trends or fine-scale curvature-driven regolith accumulation exerts greater control on shallow coseismic failure

2.2 Physical slope-stability model

ShallowLandslider evaluates coseismic slope stability using a three-dimensional extension of the Newmark sliding block method, implemented within the Landlab modelling environment. The model computes mechanical instability at each grid node based on local slope angle, regolith thickness, material strength, and seismic accelerations, and stochastically samples the mechanically unstable terrain to select discrete landslides. In this subsection, we outline the governing equations and describe how they are incorporated into the model workflow. Figure 3 provides a broad overview of the modelling workflow, with Table 1 listing all parameters used in the model, their definitions, units, and any default values.

2.2.1 Infinite-slope and Newmark formulation

The Newmark method conceptualises landslide initiation as the downslope displacement of a rigid block sliding on an infinite slope. Failure occurs when the seismic driving acceleration (a_s) exceeds the critical acceleration (a_c), the threshold required to overcome resisting forces (Jibson et al., 2000; Newmark, 1965). The critical acceleration depends on the static factor of safety (FS) and slope angle (α):

$$a_c = (FS - 1) * g \sin\alpha \tag{1}$$

The static factor of safety for a saturated regolith layer of thickness h_s is given by (Jibson et al., 2000):

$$FS = \frac{c'}{\gamma_t h_s \sin\alpha} + \frac{\tan\phi'}{\tan\alpha} - \frac{m\gamma_w \tan\phi'}{\gamma_t \tan\alpha} \tag{2}$$

where, c' is the effective cohesion, ϕ' is the angle of friction, γ_t and γ_w are the unit weights of regolith (unsaturated) and water, respectively, and m is the proportion of submerged regolith.

Under dry or partially saturated conditions, pore-water pressure effects diminish and suction enhances shear strength. In this case, FS becomes:

$$FS = \frac{c' + (\sigma_n - u_a)\tan\phi' + (u_a - u_w)\tan\phi^b}{\gamma_t h_s \sin\alpha} \tag{3}$$

where σ_n is the total normal stress, $\sigma_n - u_a$ is the net normal stress on the slip surface, u_a and u_w are pore water and air pressure, respectively, $u_a - u_w \equiv \psi$ = matric suction, and ϕ^b = angle of increase in shear strength with matric suction (Cho and Lee, 2002; Huang et al., 2020). For low saturation, $\phi^b \approx \phi'$ (Wong and Ho, 2000).

We can represent $\sigma_n = \text{weight} \times \cos\alpha$, where the weight of the sliding block is the unit weight of the regolith multiplied by the thickness of the block (weight $= \gamma_t h_s$). Additionally, since matric suction (ψ) can be written as $(u_a - u_w)$, and $u_a = 0$, equation (3) simplifies to:

$$FS = \frac{c' - \psi \tan\phi'}{\gamma_t h_s \sin\alpha} + \frac{\tan\phi'}{\tan\alpha} \tag{4}$$

Substituting equation (4) into equation (1) yields the time-independent critical acceleration required to initiate sliding of the regolith layer:

$$a_{c,constant} = \frac{c'g - \psi g \tan\phi'}{\gamma_t h_s} + g\cos\alpha \tan\phi' - g\sin\alpha \tag{5}$$

In this formulation, cohesion and regolith thickness jointly determine the depth and location of the potential failure plane, making the Newmark approach inherently sensitive to shallow, regolith-sourced failures. Variations in c' therefore act as a proxy for uncertainty in regolith fabric, root reinforcement, and matric suction, while variations in h_s directly alter the resisting mass and thus the likelihood of shallow failure. While mechanical instability (i.e., $FS \leq 1$) identifies terrain that is capable of failing under seismic loading, it does not by itself identify a realised landslide.

2.2.2 Transient seismic forcing

During an earthquake, both horizontal (a_h) and vertical (a_v) accelerations modify normal stress and driving forces. The acceleration normal to the slope is:

$$a_n = a_v(t)\cos\alpha + a_h(t)\sin\alpha,$$

and the transient critical acceleration is (Huang et al., 2020):

$$a_{c,transient}(t) = \left(\frac{c'g - g\psi\tan\phi'}{\gamma_t h_s}\right) - g\sin\alpha + \tan\phi'\left(g\cos\alpha - a_v(t)\cos\alpha - a_h(t)\sin\alpha\right) \tag{6}$$

The downslope driving acceleration $a_s(t)$ is defined as:

$$a_s(t) = a_h(t)\cos\alpha - a_v(t)\sin\alpha \tag{7}$$

A grid cell becomes a candidate for failure when $a_s(t) > a_{c,transient}(t)$. In this study, we use spatially gridded horizontal and vertical PGA components and evaluate failure potential based on peak values; time histories are used only to compute Newmark displacement, which we do not analyse further, since we focus on predicted instability patterns, not displacement magnitudes.

2.3 Model framework and implementation

ShallowLandslider organises the slope-stability calculations described above into a modular workflow that progresses from DEM preprocessing to population-level landslide realisation. Although the overall framework also includes a runout and mobility component, it is still in development. The present study focuses exclusively on the landslide-identification module, which delineates mechanically unstable terrain but does not simulate post-failure motion. In this section, we describe how the component implements these physics on a gridded landscape; how topographic attributes are calculated, how mechanically unstable terrain is grouped and partitioned into candidate slope units, and how landslides are ultimately selected through a probability-based sampler. Deterministic mechanical instability (i.e., $FS \leq 1$) is a necessary but insufficient condition for a realised landslide. This workflow (Figure 3) is implemented within the Landlab framework and is designed to ensure that physically derived instability patters are translated into realistic, spatially coherent landslide populations.

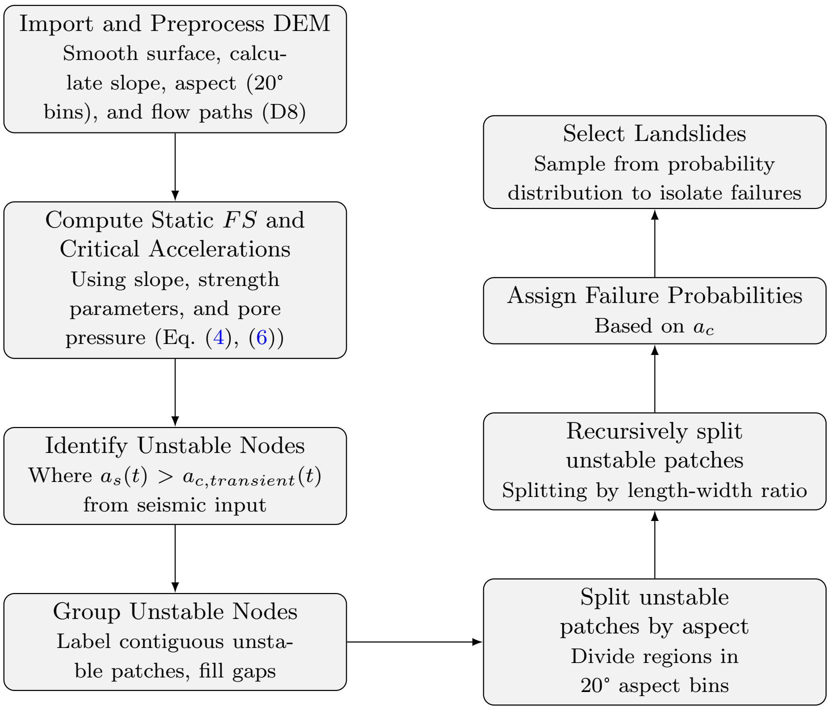

Figure 3: Workflow of *ShallowLandslider*, showing DEM preprocessing, factor-of-safety and critical-acceleration calculations, identification of unstable nodes, geometric grouping and subdivision of unstable patches, assignment of failure probabilities, and final selection of realised landslides.

2.3.1 Topography and spatial discretisation

We use a lightly smoothed 30 m SRTM DEM for each subregion as our gridded framework. To suppress pixel-scale artefacts and striping while preserving hillslope curvature, we apply a 3 × 3 median filter to the DEM prior to calculating any topographic parameters. This smoothing is optional and would not be necessary for products such as NASADEM, or MERIT, which are preprocessed to mitigate these issues, or for grids that have been smoothed by erosive processes in broader landscape evolution modelling scenarios. The 30 m resolution

DEM was selected due to its wide availability, and its balance between capturing hillslope-scale variability and computational efficiency. We computed slope, topographic aspect, and planform curvature at each grid node for use in stability calculations and regolith thickness parameterisations (Figure 3). Planform curvature was calculated using the RichDEM implementation of the Zevenbergen and Thorne (1987) method, which fits a quadratic surface to each grid cell and its neighbours and computes curvature perpendicular to the maximum slope direction. Flow routing uses D8 connectivity to obtain contributing drainage area where required.

2.3.2 Regolith thickness parameterisation

We implemented five regolith-thickness parameterisations to evaluate how different geomorphic assumptions about colluvial storage influence predicted patterns of coseismic shallow landsliding, with each formulation representing a distinct hypothesis about how regolith accumulates across steep Himalayan terrain. The simplest configuration applies a uniform, constant regolith depth of $h_s = 1\,\mathrm{m}$ across the DEM. This baseline scenario provides a reference against which more realistic spatial variations can be assessed, although it necessarily ignores natural heterogeneity in regolith production, transport, and erosion. To incorporate broad-scale hypsometric structure, the inverse elevation-dependent parameterisation imposes a linear decrease in regolith depth with height, from a maximum of $h_{s,\max} = 1.5\,\mathrm{m}$ in valley positions to $h_{s,\min} = 0\,\mathrm{m}$ at the highest elevations. This design reflects well-documented patterns of regolith thinning on steep ridges, where enhanced erosion and reduced deposition limit colluvial accumulation (Dietrich et al., 1995; Li et al., 2017; Pelletier and Rasmussen, 2009).

A second class of parameterisations focuses on topographic convergence. In the drainage-area-dependent formulation, regolith thickness is scaled to the upstream contributing area derived from flow routing, such that nodes in hollows and valley floors acquire thicker colluvial packages, whereas divergent slopes and ridgelines remain thin. This approach reflects the geomorphic tendency for sediment to accumulate in convergent topography, linking regolith thickness directly to hillslope transport pathways and hydrologic connectivity (Catani et al., 2010; Dietrich et al., 1995; Park et al., 2001; Parker et al., 2016). Similarly, the curvature-dependent parameterisation assigns regolith thickness as a function of planform curvature κ. Classical hillslope soil-production models (Dietrich et al., 1995; Heimsath et al., 1997) relate h_s to curvature through a non-linear logarithmic expression $\left(h_s(\kappa) = -h_* \ln \frac{D_\kappa}{P_0}\right)$, which captures the rapid thickening of regolith in concave hollows and its thinning on convex slopes. However, because the logarithmic term diverges for $\kappa \leq 0$, the formulation requires piecewise definitions and can be difficult to apply consistently across large, heterogeneous landscapes. Following Patton et al. (2018), we therefore adopt a linear approximation, $h_s = \bar{h} + \beta\kappa$. Here, $\bar{h} = 1\,\mathrm{m}$ is set *a priori* and the slope coefficient $\beta = -446.3, \sigma_\kappa + 30.3$ is derived from a local (5-cell) standard deviation of curvature. To avoid unrealistically thick or negative depths in strongly concave or convex areas, values are clipped to the range 0-1.5 m. This approximation preserves the essential geometric dependence of regolith storage on curvature while enabling stable regional-scale application.

Finally, to combine large-scale hypsometric control with fine-scale topographic variability, we constructed an elevation-weighted curvature parameterisation in which regolith thickness is computed as the mean of the elevation-dependent estimate $h_{s,\text{elev}}$ and the curvature-derived value $h_{s,\kappa}$. This hybrid formulation imposes gradual thinning of regolith toward high ridges while incorporating the local effects of hillslope convergence and divergence. As with the other parameterisations, depths are clipped to 0-1.5 m to maintain physical plausibility. All five configurations were applied in both study areas to assess how different assumptions about the spatial organisation of h_s influence coseismic instability under varying topographic and seismic conditions. Model performance was evaluated using the KS, Kuiper, and Wasserstein metrics for landslide area, mean elevation, mean slope, and aspect.

2.3.3 Material strength and cohesion

Effective cohesion (c') and the angle of internal friction (ϕ') govern the shear resistance of the regolith in the infinite-slope formulation (Equations (2)–(6); Table 1). To isolate the interaction between regolith architecture and material strength, we vary c' systematically over a plausible shallow-regolith range (0–20 kPa) for each regolith-depth structure while holding other parameters fixed within representative regional values (Campforts et al., 2022; Huang et al., 2020). ϕ' is held constant at 30° to avoid covariance with c', ensuring that differences in modelled landslide populations arise primarily from the combined effects of regolith thickness (h_s) and cohesion. This design emphasises the depth-sensitivity of shallow failures: lower cohesion values reduce shear resistance and promote failure in thinner regolith, whereas higher cohesion suppresses failure except in locally thicker or steeper terrain. Although we hold ϕ' constant, we note that varying the friction angle would primarily shift the range of slope angles susceptible to failure. All other mechanical parameters follow standard regional values (Table 1).

2.3.4 Simulating landslide populations

Because mechanically unstable terrain often forms spatially extensive, connected patches when evaluated on DEM grids, we apply a population-based geometrical partitioning to divide them into discrete candidate landslides, ensuring consistency with empirical distributions of landslide size and shape. This hybrid physical-statistical design targets population-level characteristics (e.g., size distributions, elevation-slope preferences) rather than pixel-scale prediction. From the set of mechanically unstable nodes, we generate discrete landslides through two sequential steps: (i) geometric partitioning of unstable terrain into candidate failures, and (ii) probabilistic sampling to reflect unresolved uncertainty in material properties and localised triggering (Figures 3, 4):

1. **Region splitting:** Unstable nodes are first grouped into contiguous regions based on spatial connectivity. To avoid patches having artificial connections across channels and ridgelines, they are split into smaller patches based on topographic aspect, essentially isolating single slope faces. Connected unstable regions are subsequently subdivided according to these aspect zones to yield candidate landslide areas. The downslope length and cross-slope width of each resulting patch are then compared to the empirical length-width

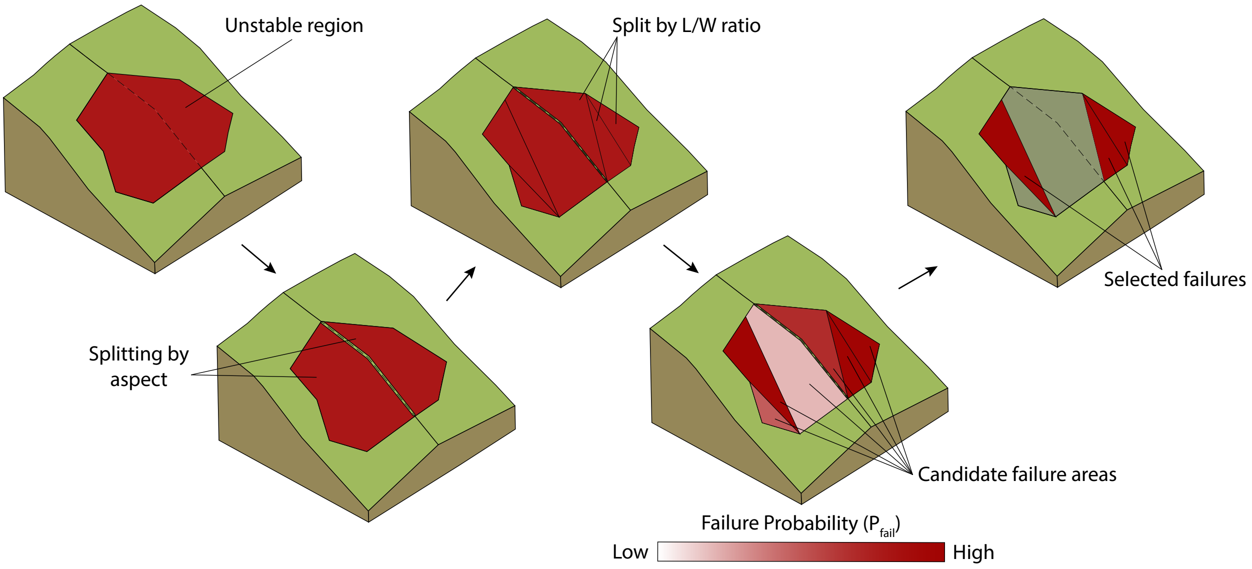

Figure 4: Schematic of the landslide-population selection workflow. Unstable nodes identified from the Newmark-based stability analysis are grouped into contiguous regions, subdivided by slope-aspect zones to isolate individual slope faces, and iteratively split using empirical length–width constraints. Each candidate patch is then assigned a failure probability based on its median a_c, and realised landslides are obtained through weighted stochastic sampling.

distribution of the mapped landslide inventory. Patches falling outside this distribution, either where width exceeds length, or where lengths are disproportionately large, are split at their centroid. This process is applied recursively: after each split, the dimensions of all subregions are recalculated, and those still falling outside the empirical range are split again, until at least *75%* of areas conform to the observed length-width relationship. This procedure constrains modelled landslides to realistic slope-parallel shapes and ensures that failures occupy discrete hillslope elements rather than DEM-connected artefacts.

2. **Stochastic sampling:** While the static factor of safety of a slope can be readily calculated, the dynamic processes of triggering and the spatial and temporal variability in strength cannot be determined using the static Mohr-Coulomb method. Therefore, we introduce a stochastic sampling component, where each candidate region is assigned a failure probability (P_{fail}) inversely proportional to its median critical acceleration. Therefore, regions with high critical acceleration (i.e., requiring a higher PGA to overcome the frictional forces) would have lower P_{fail}, and vice versa. The median critical acceleration is a robust measure of resistance that biases selection toward mechanically more failure-prone regions while preserving variability. A weighted sampler then selects a subset of candidate regions as landslides; the selection proportion reflects both the mean and spread of the probability field ($\overline{P_{fail}} + \sigma_{P_{fail}}$), ensuring that the number of selected landslides reflects both central tendency and variability in P_{fail}. This approach introduces some stochasticity while biasing the selection toward areas more likely to fail.

In traditional Newmark analyses, the Newmark displacement is usually calculated after identifying unstable areas (Huang et al., 2020; Jibson et al., 2000). However, in this paper, we emphasise the spatial patterns of instability rather than on post-failure deformation magnitudes.

2.4 Simulation ensemble and validation metrics

We evaluate model behaviour using an ensemble that spans the regolith-thickness parameterisations described in Section 2.3.2 and a range of cohesion values ($c' = 0$–$20\,\mathrm{kPa}$). All other mechanical and seismic parameters are held fixed across runs. Simulations are performed on 30 m grids for each subregion.

Landslide inventory data : The observed dataset is the coseismic landslide inventory compiled by Roback et al. (2018). The authors mapped over 24,000 coseismic landslides triggered by the Gorkha earthquake and its aftershocks across central Nepal. The inventory was derived from pre- and post-earthquake high-resolution optical imagery (WorldView-2, -3 and Pleiades), manually delineated at a general ground sample distance of 20 cm – 50 cm. The dataset is made up of polygonal landslide outlines, classified by failure type and location accuracy. For our analysis, we clipped the inventory to the two subregions used in our model simulations and rasterized the polygons to the 30 m grid resolution of the input DEM. We excluded polygons that were smaller than a single grid cell, since our model is restricted to the pixel resolution of the DEM. The resulting raster layers were used to calculate the magnitude-frequency statistics, along with the spatial distribution of the observed landslides across elevation, slope, and aspect.

Population-level comparison metrics : To quantify the similarity between the modelled and observed landslide distributions, we used two complementary non-parametric statistics: the Kolmogorov–Smirnov (KS) / Kuiper statistic, and the Wasserstein distance. These metrics compare entire probability distributions rather than discrete observations, making them well-suited for evaluating the performance of models designed to reproduce overall distributional characteristics. The KS test quantifies the maximum difference between cumulative distributions and is applied to linear variables (area, elevation, slope), while its circular analogue, the Kuiper statistic, is used for topographic aspect (Fisher, 1993). The Wasserstein distance provides a complementary measure of overall distributional offset and is widely used in geomorphology and image-comparison contexts (Rubner et al., 2000). We computed these metrics for four key variables that collectively describe the statistical structure of the landslide population: landslide area, mean elevation, mean slope, and mean aspect. Each of these statistical comparisons were performed on normalised cumulative distributions to eliminate scale effects between variables.

3 Results

3.1 Influence of regolith-thickness parameterisation

We evaluate four primary regolith-thickness parameterisations across both study areas: (i) Uniform 1 m; (ii) Inverse-elevation; (iii) Curvature-dependent; and (iv) Elevation-weighted Curvature. The fifth configuration,

Table 1: Notation and symbols used in *ShallowLandslider*

Symbol	**Description**	**Default Value (if any)**
Geometric Parameters		
α	Slope angle (°)	–
h_s	Regolith thickness in normal direction (m)	–
m	Proportion of submerged regolith	0.5
Strength Parameters		
c'	Effective cohesion (Pa)	–
ϕ'	Effective angle of friction (°)	30
ϕ^b	Angle of increase in shear strength with matric suction (°)	–
FS	Static factor of safety	1.0
Unit Weight		
γ_t	Unit weight of regolith ($\mathrm{kN\,m^{-3}}$)	15
γ_w	Unit weight of water ($\mathrm{kN\,m^{-3}}$)	9.81
Stress and Pore Pressure (Pa)		
σ_n	Total normal stress	–
$\sigma_n - u_a$	Net normal stress on the slip surface	–
u_a	Pore air pressure	0
u_w	Pore water pressure	–
ψ	Matric suction ($u_a - u_w$)	–
u	Pore pressure replacement for ψ ($m\gamma_w h$)	–
Seismic Parameters ($\mathrm{m\,s^{-2}}$)		
g	Acceleration due to gravity	9.81
a_c	Critical acceleration	–
$a_{c,transient}$	Critical transient acceleration	–
a_s	Sliding acceleration	–
a_n	Acceleration normal to the slope	–
a_h, a_v	Horizontal/vertical acceleration (PGA)	–

upstream drainage area-dependent, is not shown here due to its intermediate results, largely similar to that of the curvature-only configurations. Distributional agreement with the Roback et al. (2018) inventory is assessed using ECDFs (Empirical Cumulative Distribution Functions) and histograms (Figures 5-6) and summarised using Kolmogorov-Smirnov (KS), Kuiper (for aspect), and Wasserstein distances (Figures 7-8).

3.1.1 Uniform 1 m regolith thickness

The uniform-depth scenario consistently performed poorest in both subregions. Predicted failures occur widely across slopes and lack the spatial organisation seen in the mapped inventory. In Subregion 1, this configuration predicts landslides that are generally too large, and at considerably higher elevations than observed in the mapped dataset, leading to broad mismatches in elevation, slope, and area distributions (e.g., area KS $\approx 0.40-0.46$; slope KS $\approx 0.20-0.30$), with Wasserstein distances similarly elevated (0.55-0.70), and aspect correspondence weak (Kuiper $\approx 0.20-0.27$; Figures 5A, 7). A similarly diffuse pattern emerges in Subregion 2, with landslides predicted to be considerably larger than those mapped, with area KS values commonly > 0.45 and large Wasserstein distances (0.30-0.70) (Figures 6, 8). This confirms that a spatially homogeneous regolith field is unable to reproduce the observed heterogeneity in either landscape, and therefore, this configuration serves as a baseline scenario.

3.1.2 Inverse-elevation-based regolith thickness

In Subregion 1, where relief is extremely high and ridgelines are dominated by exposed bedrock, the inverse-elevation based parameterisation performs substantially better. Imposing a systematic thinning of regolith with elevation produces a failure pattern concentrated on lower- and mid-slope positions, closely matching the mapped hypsometric structure. Slope-elevation relations are reproduced most faithfully at cohesion values of approximately 10 kPa, where predicted failures align with the observed concentration of slides on steep, but not extreme, slopes (elevation $KS = 0.095$, slope $KS = 0.084$), and corresponding Wasserstein distances (W)= 0.071 (elevation) and 0.104 (slope). Although predicted landslides tend to remain larger than observed (area $KS \approx 0.45$, $W \approx 0.28 - 0.44$), the overall spatial distribution is consistent with a landscape where colluvial material becomes increasingly limited toward high ridges (Figures 5B; 7). In Subregion 2, however, elevation alone does not organise regolith thickness effectively. Area and slope mismatches are moderate to large (e.g., area $KS \approx 0.50$, $W \approx 0.27 - 0.49$; slope $KS \approx 0.17 - 0.26$), and aspect correspondence is consistently poorer compared to curvature-modulated approaches (Figures 6B; 8).

3.1.3 Curvature-based regolith thickness

Curvature-based regolith thickness emphasise local convergence and divergence of hillslopes, producing more realistic clustering of unstable terrain, particularly in Subregion 2. In Subregion 1, curvature-only models reproduced area and slope distributions well (area $KS \approx 0.11 - 0.26$; slope $KS \approx 0.20 - 0.24$), but overpredicts landslides at higher elevations than observed (elevation $KS > 0.45$). Aspect correspondence was intermediate (Kuiper $\approx 0.20 - 0.23$), better than Uniform but weaker than Inverse-elevation (Figures 5, 7). This suggests that while curvature captures local hillslope structure, it does not control the primary topographic trends driving landsliding in this region. However, curvature-only models performed far better in Subregion 2. This landscape contains abundant regolith-mantled hollows and valley-parallel convergent slopes, and the curvature-based parameterisation successfully localises failures in these features, with predicted landslides having very appropriate sizes (area $KS \approx 0.11 - 0.19$), and matching the elevation, slope, and aspect distributions of the mapped landslides extremely well (elevation $KS \approx 0.17 - 0.24$, slope $KS \leq 0.10$, aspect Kuiper$\approx 0.20 - 0.22$), all of which are better than any of the purely elevation-based formulations (Figures 6, 8). Taken together, these results reflect the strong geomorphic influence of planform convergence in shaping landslide patterns, while also showing that it is not always the primary control.

3.1.4 Elevation-weighted Curvature-based regolith thickness

The hybrid parameterisation, which couples broad-scale elevation trends with local curvature variability, provides the most balanced representation across both landscapes. In Subregion 1, this approach, combined with $c' = 15$ kPa improves area (area $KS \approx 0.19$) and slope (slope $KS = 0.089$) distributions compared to curvature alone while still reflecting reduced colluvial storage at high elevations. However, similar to the curvature-only parameterisation, landslides were still predicted at significantly higher elevations than mapped (elevation $KS \approx 0.48$), and aspect performance, while moderate (Kuiper $\approx 0.20 - 0.23$), did not surpass the Inverse-elevation-based approach (Figures 5C; 7).

In Subregion 2, this combined formulation yields the closest overall match to the mapped population. It captures the observed pattern of failures concentrated in concave, regolith-rich hollows while still respecting the gentle elevation gradient of this landscape. At $c' = 15\,\text{kPa}$, slope preferences, elevation clustering, and aspect organisation are all represented with high fidelity (area $KS = 0.3$, $W = 0.165$; elevation $KS = 0.167$, $W = 0.183$; slope $KS = 0.065$, $W = 0.071$; aspect kuiper$= 0.192$, with a mean aspect deviation of approximately $37°$). Taken together, these values make the elevation-weighted curvature configuration the best-performing model for Subregion 2, providing the most coherent multi-metric match to the observed coseismic landslide population (Figures 6C; 8).

3.2 Influence of cohesion

Across all regolith-thickness parameterisations and in both subregions, model behaviour shows a consistent sensitivity to effective cohesion. At low cohesion ($c' = 0$–$5\,\text{kPa}$), the model predicts widespread instability, generating unrealistically high numbers of failures across the entire elevation and slope range, with marked increses in both KS and Wasserstein distances. At high cohesion ($c' \approx 20\,\text{kPa}$), instability is strongly suppressed, yielding too few failures compared to the inventory. This pattern emerges in both subregions (e.g., Subregion 1: elevation KS $= 0.095$ at $c' = 15\,\text{kPa}$ vs. ≥ 0.45 for $c' = 0\,\text{kPa}$; Subregion 2: slope $KS = 0.065$ at $c' = 15\,\text{kPa}$ vs. $KS = 0.183 - 0.246$ at $c' = 0 - 5\,\text{kPa}$).

Intermediate cohesion values of $c' \approx 10$–$15\,\text{kPa}$ produce the closest distributional agreement with the mapped landslide populations (Figures 5, 6). This narrow optimal range is consistent with shallow, regolith-sourced failures (Montgomery and Dietrich, 1994) and supports the sensitivity of the model to realistic strength values.

3.3 Subregional contrasts

The ensemble reveals consistent but contrasting controls on coseismic landsliding in the two landscapes. In Subregion 1, the Inverse-elevation parameterisation provides the closest match to the mapped population across elevation, slope, and aspect, with curvature-based models performing less well, particularly for elevation distributions (Figures 5, 7). In contrast, in Subregion 2, curvature-informed parameterisations, especially the Elevation-weighted Curvature model, produce the lowest KS and Wasserstein distances for area, elevation, and slope, along with the strongest correspondence in aspect (Figures 6C; 8).

Across the full ensemble, these results show that the dominant controls differ between the landscapes: Subregion 1 is best reproduced by parameterisations emphasising large-scale elevation structure, whereas Subregion 2 aligns most closely with models incorporating curvature-driven local variability. Although the optimal cohesion range is similar across both subregions (Section 3.2), the performance of each regolith-thickness parameterisation is landscape-specific, reflecting differences in the spatial correspondence between the modelled regolith structure and the mapped landslide distributions.

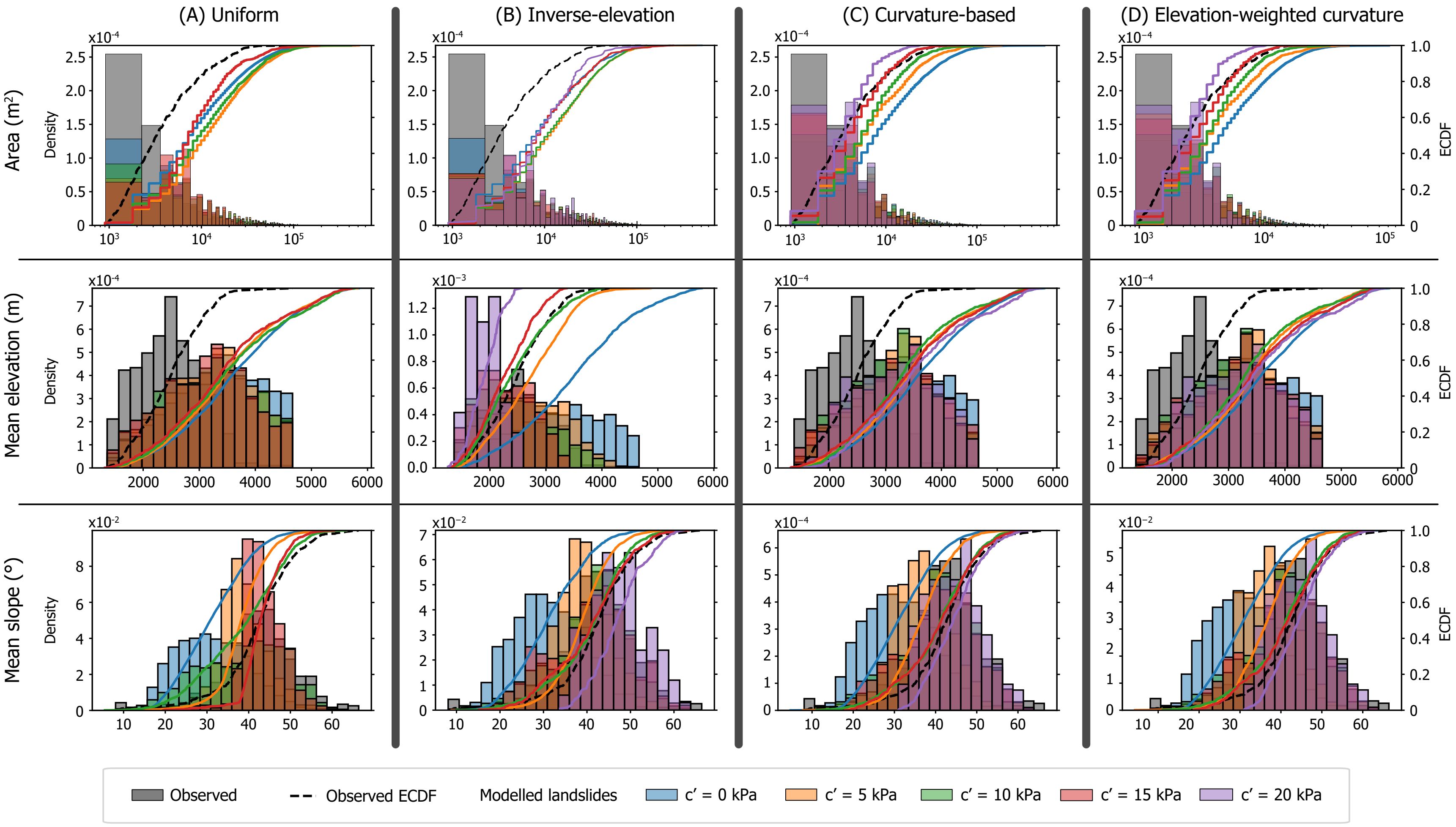

Figure 5: Histograms and empirical cumulative distribution functions (ECDFs) for each model run in Subregion 1. (A) Uniform 1 m regolith depth, (B) Inverse-elevation dependent, (C) Curvature-dependent, (D) Elevation-weighted Curvature-dependent. Grey histograms and dashed black lines show observed landslide distributions; coloured curves show results for different cohesion values.

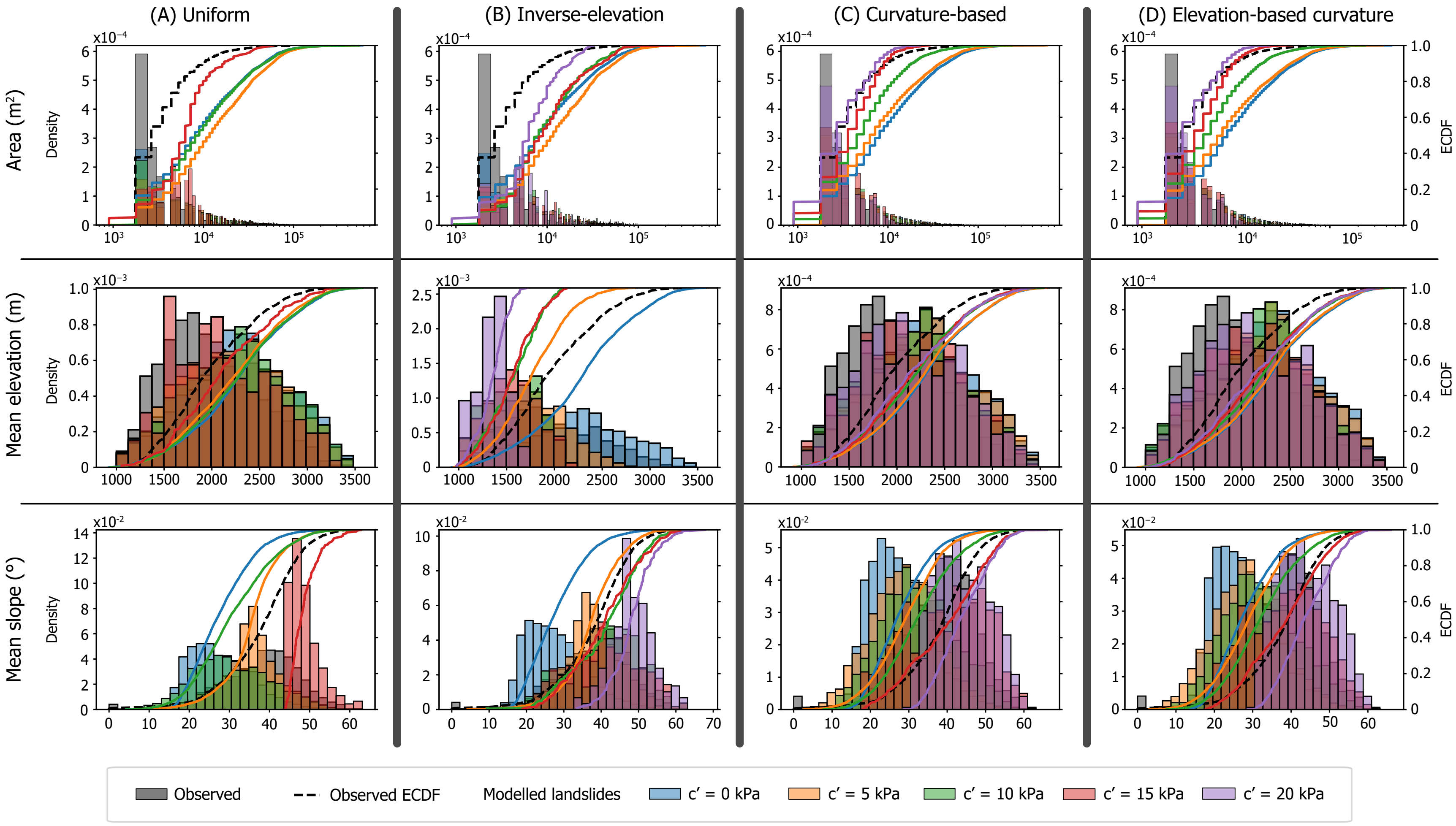

Figure 6: Histograms and empirical cumulative distribution functions (ECDFs) for each model run in Subregion 2. (A) Uniform 1 m regolith depth, (B) Inverse-elevation dependent, (C) Curvature-dependent, (D) Elevation-weighted Curvature-dependent. Grey histograms and dashed black lines show observed landslide distributions; coloured curves show results for different cohesion values.

4 Discussion

ShallowLandslider reproduces key statistical and spatial characteristics of regional coseismic shallow landslide populations by combining physically derived stability with population-level realisation. Across the ensemble, regolith-thickness parameterisations that impose physically plausible spatial variability, including elevation trends, curvature-driven convergence, or a combination of both, consistently outperform a uniform-depth baseline. The uniform case fails to capture observed clustering or topographic preferences, underscoring the need to represent realistic subsurface structure at landscape scale.

Moderate effective cohesion ($c' \approx 10$–$15\,\mathrm{kPa}$) yields the closest overall agreement with the mapped inventories in both subregions. Lower cohesion values lead to widespread overprediction of failures, whereas higher values suppress failure almost entirely. Although cohesion influences the total number and the elevation and slope distributions of failures, the dominant control on population structure arises from the spatial organisation of regolith thickness. The strongest matches occur when the regolith-thickness parameterisation captures the landscape-scale patterns that influence coseismic susceptibility in each subregion.

A core feature of the framework is its emphasis on population-level agreement. Rather than attempting pixel-scale prediction, which is not expected or required for regional coseismic landslide modelling, the approach evaluates distributional similarity in area, elevation, slope, and aspect. These metrics summarise the structural organisation of landslide populations and provide a basis for interpreting how landscape morphology and regolith structure interact under similar seismic forcing.

4.1 Contrasting landscape controls across subregions

The distribution of coseismic shallow landslides suggests that regolith thicknesses in each subregion follow different models. In Subregion 1, the Inverse-elevation parameterisation provides the closest correspondence across slope, elevation, and aspect, and this suggests that broad hypsometric trends, particularly thinning of regolith toward higher ridges, play a primary role in shaping coseismic failure patterns. Curvature-only parameterisations improve area distributions but do not reproduce the observed elevation and slope preferences as effectively.

In Subregion 2, curvature-based model parameterisation best match the areal distributions as well as the elevation and slope distributions. Applying an elevation weighting to the curvature based models improves the fit to these metrics. In this landscape, fine-scale planform convergence appears to exert a stronger influence on landslide clustering, slope preferences, and aspect distributions than broad hypsometric patterns. This behaviour is consistent across the range of cohesions that we tested, indicating that cohesion modulates overall failure propensity but does not override the dominant influence of regolith-structure parameterisation.

The difference in the success of different regolith thickness parameterisations suggests that there may be a change in process-dominance between the two subregions, likely due to the presence or absence of a soil mantle. Subregion 2 can be parameterised by curvature-based regolith thickness distributions commonly found

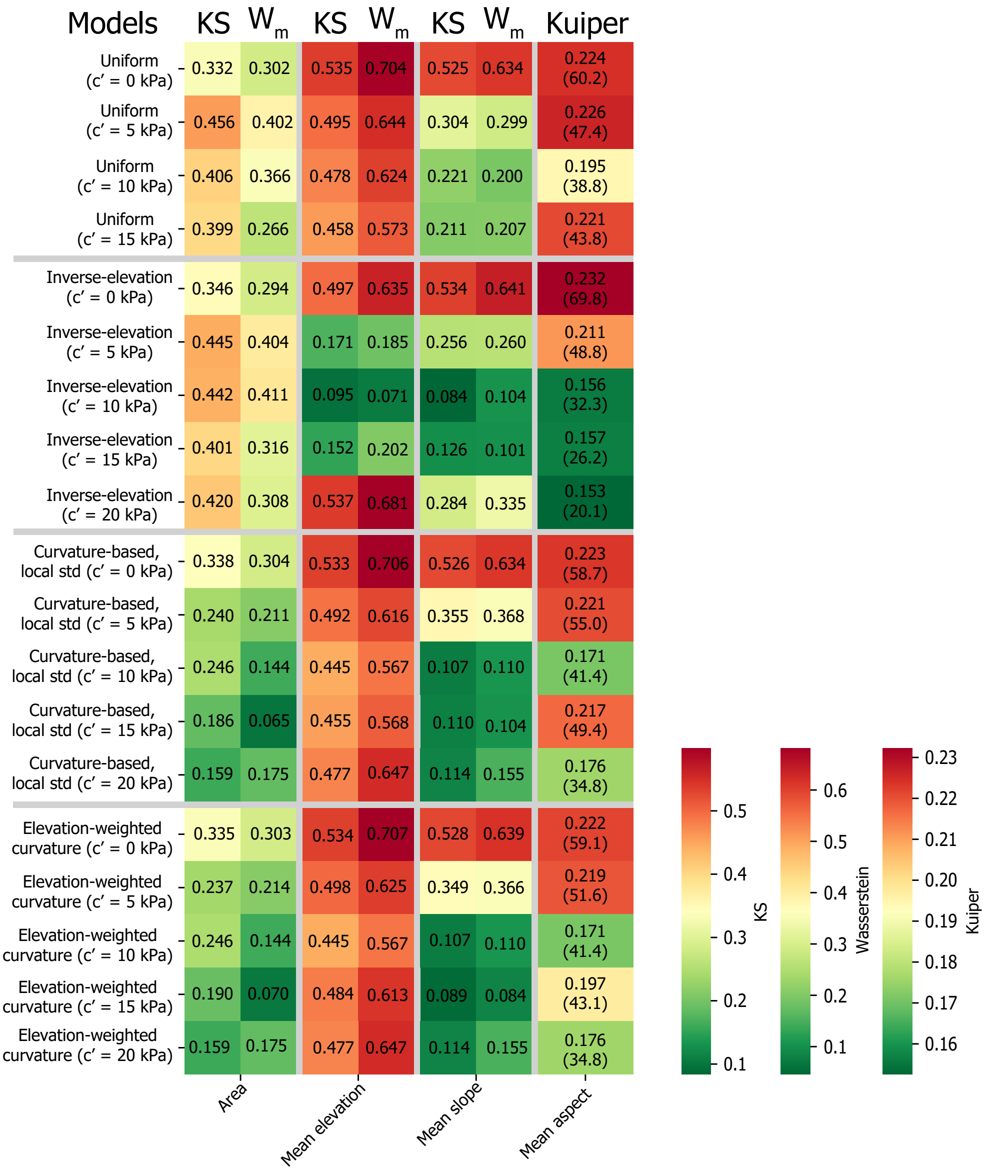

Models	Area		Mean elevation		Mean slope		Mean aspect
	KS	W_m	KS	W_m	KS	W_m	Kuiper
Uniform (c′ = 0 kPa)	0.332	0.302	0.535	0.704	0.525	0.634	0.224 (60.2)
Uniform (c′ = 5 kPa)	0.456	0.402	0.495	0.644	0.304	0.299	0.226 (47.4)
Uniform (c′ = 10 kPa)	0.406	0.366	0.478	0.624	0.221	0.200	0.195 (38.8)
Uniform (c′ = 15 kPa)	0.399	0.266	0.458	0.573	0.211	0.207	0.221 (43.8)
Inverse-elevation (c′ = 0 kPa)	0.346	0.294	0.497	0.635	0.534	0.641	0.232 (69.8)
Inverse-elevation (c′ = 5 kPa)	0.445	0.404	0.171	0.185	0.256	0.260	0.211 (48.8)
Inverse-elevation (c′ = 10 kPa)	0.442	0.411	0.095	0.071	0.084	0.104	0.156 (32.3)
Inverse-elevation (c′ = 15 kPa)	0.401	0.316	0.152	0.202	0.126	0.101	0.157 (26.2)
Inverse-elevation (c′ = 20 kPa)	0.420	0.308	0.537	0.681	0.284	0.335	0.153 (20.1)
Curvature-based, local std (c′ = 0 kPa)	0.338	0.304	0.533	0.706	0.526	0.634	0.223 (58.7)
Curvature-based, local std (c′ = 5 kPa)	0.240	0.211	0.492	0.616	0.355	0.368	0.221 (55.0)
Curvature-based, local std (c′ = 10 kPa)	0.246	0.144	0.445	0.567	0.107	0.110	0.171 (41.4)
Curvature-based, local std (c′ = 15 kPa)	0.186	0.065	0.455	0.568	0.110	0.104	0.217 (49.4)
Curvature-based, local std (c′ = 20 kPa)	0.159	0.175	0.477	0.647	0.114	0.155	0.176 (34.8)
Elevation-weighted curvature (c′ = 0 kPa)	0.335	0.303	0.534	0.707	0.528	0.639	0.222 (59.1)
Elevation-weighted curvature (c′ = 5 kPa)	0.237	0.214	0.498	0.625	0.349	0.366	0.219 (51.6)
Elevation-weighted curvature (c′ = 10 kPa)	0.246	0.144	0.445	0.567	0.107	0.110	0.171 (41.4)
Elevation-weighted curvature (c′ = 15 kPa)	0.190	0.070	0.484	0.613	0.089	0.084	0.197 (43.1)
Elevation-weighted curvature (c′ = 20 kPa)	0.159	0.175	0.477	0.647	0.114	0.155	0.176 (34.8)

Figure 7: Model performance heatmaps for subregion 1, comparing modelled and observed distributions of landslide area, elevation, slope, and aspect. Colours show Kolmogorov–Smirnov and Wasserstein distances for linear variables and the Kuiper statistic for aspect. Values are shown for all regolith-thickness parameterisations and cohesion values..

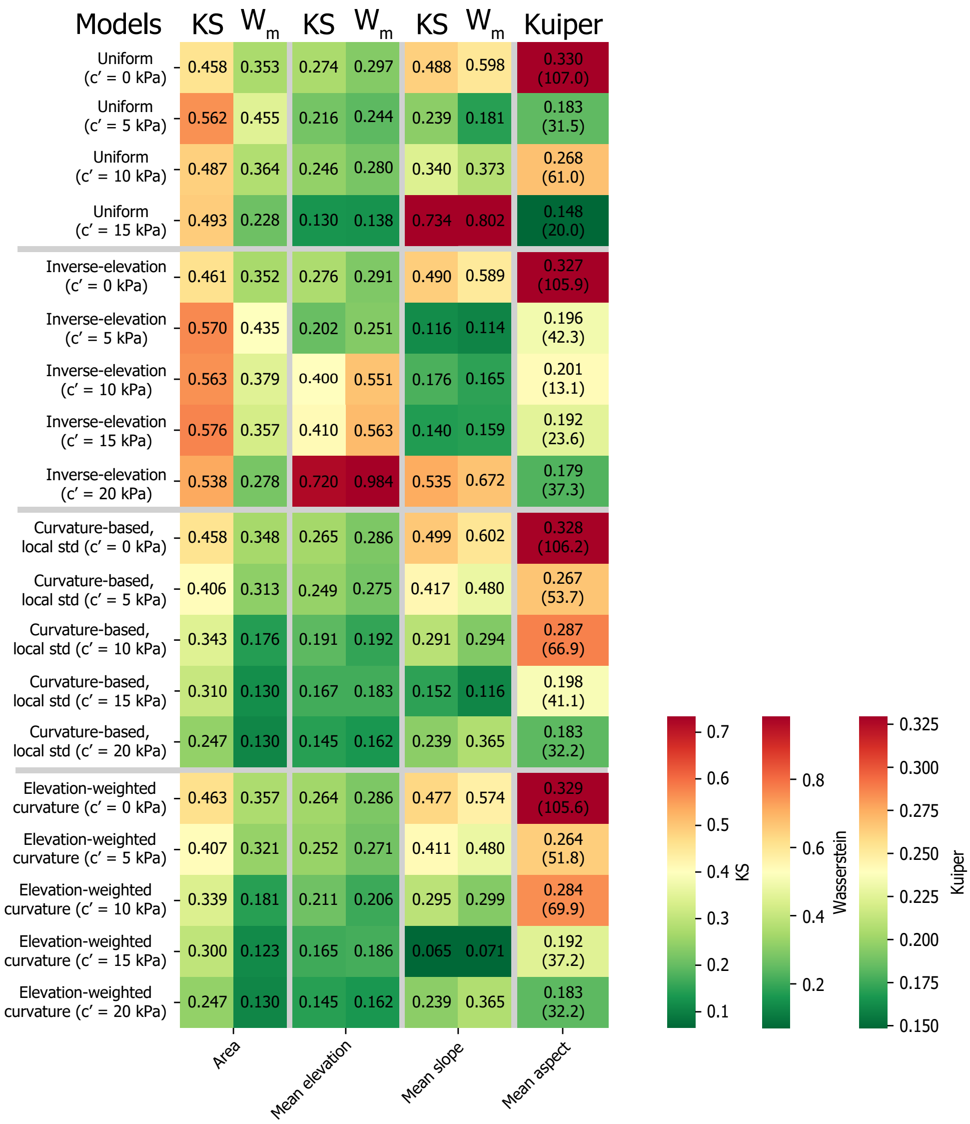

Models	KS	W_m	KS	W_m	KS	W_m	Kuiper
Uniform (c′ = 0 kPa)	0.458	0.353	0.274	0.297	0.488	0.598	0.330 (107.0)
Uniform (c′ = 5 kPa)	0.562	0.455	0.216	0.244	0.239	0.181	0.183 (31.5)
Uniform (c′ = 10 kPa)	0.487	0.364	0.246	0.280	0.340	0.373	0.268 (61.0)
Uniform (c′ = 15 kPa)	0.493	0.228	0.130	0.138	0.734	0.802	0.148 (20.0)
Inverse-elevation (c′ = 0 kPa)	0.461	0.352	0.276	0.291	0.490	0.589	0.327 (105.9)
Inverse-elevation (c′ = 5 kPa)	0.570	0.435	0.202	0.251	0.116	0.114	0.196 (42.3)
Inverse-elevation (c′ = 10 kPa)	0.563	0.379	0.400	0.551	0.176	0.165	0.201 (13.1)
Inverse-elevation (c′ = 15 kPa)	0.576	0.357	0.410	0.563	0.140	0.159	0.192 (23.6)
Inverse-elevation (c′ = 20 kPa)	0.538	0.278	0.720	0.984	0.535	0.672	0.179 (37.3)
Curvature-based, local std (c′ = 0 kPa)	0.458	0.348	0.265	0.286	0.499	0.602	0.328 (106.2)
Curvature-based, local std (c′ = 5 kPa)	0.406	0.313	0.249	0.275	0.417	0.480	0.267 (53.7)
Curvature-based, local std (c′ = 10 kPa)	0.343	0.176	0.191	0.192	0.291	0.294	0.287 (66.9)
Curvature-based, local std (c′ = 15 kPa)	0.310	0.130	0.167	0.183	0.152	0.116	0.198 (41.1)
Curvature-based, local std (c′ = 20 kPa)	0.247	0.130	0.145	0.162	0.239	0.365	0.183 (32.2)
Elevation-weighted curvature (c′ = 0 kPa)	0.463	0.357	0.264	0.286	0.477	0.574	0.329 (105.6)
Elevation-weighted curvature (c′ = 5 kPa)	0.407	0.321	0.252	0.271	0.411	0.480	0.264 (51.8)
Elevation-weighted curvature (c′ = 10 kPa)	0.339	0.181	0.211	0.206	0.295	0.299	0.284 (69.9)
Elevation-weighted curvature (c′ = 15 kPa)	0.300	0.123	0.165	0.186	0.065	0.071	0.192 (37.2)
Elevation-weighted curvature (c′ = 20 kPa)	0.247	0.130	0.145	0.162	0.239	0.365	0.183 (32.2)
	Area		Mean elevation		Mean slope		Mean aspect

Figure 8: Model performance heatmaps for subregion 2, comparing modelled and observed distributions of landslide area, elevation, slope, and aspect. Colours show Kolmogorov–Smirnov and Wasserstein distances for linear variables and the Kuiper statistic for aspect. Values are shown for all regolith-thickness parameterisations and cohesion values.

in soil-mantled landscapes. It shows rolling, regolith-mantled terrain, lower overall relief (2712 m; Figure 2i). In contrast, Subregion 1 has extremely thin soils on ridges and a distribution of regolith thicknesses that can only partially be modelled based on curvature. This is consistent with the presence of extensive exposed bedrock, steep ridgelines, and very high relief (4626 m; Figure 2ii).

4.2 Evidence for shallow coseismic landsliding

Multiple lines of evidence from the model ensemble, together with established observations of the 2015 Gorkha earthquake, indicate that most coseismic landslides were shallow and sourced from near-surface regolith. First, the optimal cohesion range that provides the closest agreement with the mapped inventory is consistently $c' \approx 10$–15 kPa across all regolith-thickness parameterisations and in both subregions. These values are characteristic of loose colluvium and mobile regolith rather than saprolite or bedrock (Cho and Lee, 2002; Wong and Ho, 2000). The strong overprediction of failures at very low cohesion and suppression of failures at high cohesion supports the interpretation that observed failures occupy a narrow mechanical window typical of shallow sliding surfaces.

Second, model performance is most sensitive to the spatial organisation of near-surface regolith. Parameterisations that encode realistic variability in regolith thickness, whether driven by elevation or curvature, consistently outperform the uniform-depth model. This behaviour indicates that failures initiate where thin, topographically structured layers of regolith overlie steep slopes, a pattern consistent with shallow failure processes. Third, the mapped Gorkha landslides themselves exhibit characteristics typical of shallow translational failures. They are generally small to moderate in area, concentrated in concave hollows and mid to lower hillslope positions, and display strong dependence on local slope and aspect (Roback et al., 2018). The enhanced model sensitivity to curvature in Subregion 2 further reinforces the importance of near-surface material organisation.

A further consideration is the potential incompleteness of landslide mapping at higher elevations. Most post-event inventories rely on spectral and vegetation-based change detection; in sparsely-vegetated, bare alpine terrain this can reduce detectability and bias mapped elevation distributions downward. Reviews of Nepal landslide inventories highlight uneven spatial coverage and methodological constraints that can under-represent particular terrain zones (Harvey et al., 2024). Moreover, Roback et al. (2018) emphasise that landslide density tracks earthquake source characteristics and rupture geometry, which places higher densities away from some of the highest ridges. These points indicate that while some under-representation of high-elevation disturbances is possible, the mapped pattern also aligns with expected shaking distributions, so incomplete detection is best considered as one of several plausible contributors to the Subregion 1 mismatch. Finally, the Gorkha earthquake also triggered a smaller number of bedrock landslides, including several large rock avalanches and deep-seated failures (Kargel et al., 2015; Meena and Tavakkoli Piralilou, 2019). These failure types are governed by structural discontinuities, lithologic contrasts, and deep mechanical conditions that are not represented in the shallow-regolith framework used here (Campforts et al., 2022). As a result, the model does not capture these bedrock-dominated failures, and their presence introduces residual mismatch between the observed and modelled landslide distributions. This limitation is particularly relevant for explaining discrepancies in the upper tail of the area distribution and in high-relief terrain where bedrock failures occurred within otherwise thinly mantled landscapes.

These lines of evidence indicate that the majority of landslides mobilised by the Gorkha earthquake were shallow and regolith-sourced, with spatial patterns governed primarily by near-surface material organisation or distances from areas of strongest shaking. The minority population of bedrock landslides, which the model does not represent, provides an additional source of natural uncertainty that contributes to the imperfect agreement between modelled and observed distributions.

4.3 Exploring potential explanations for subregional contrasts

The contrasting performance of the regolith-thickness parameterisations between subregions 1 and 2 raises the question of what controls these differences. Several intuitive explanations can be considered, and the ensemble results allow us to evaluate their plausibility. One possibility is that uncertainties in shallow-failure mechanics limit the ability of the model to reproduce observed landslide patterns. However, a narrow and physically realistic cohesion range yields the closest matches in both landscapes, which indicates that the underlying physics operate consistently and are unlikely to explain the differing model behaviour. A second possibility is that limitations in DEM resolution or model resolution produce discrepancies between the landscapes. If this were the case, all parameterisations would behave similarly across both subregions, since the same grid and preprocessing procedures were applied throughout. The ensemble instead reveals systematic differences and even reversals in performance between parameterisations, which suggests that resolution alone cannot account for the contrasting outcomes. A third possibility is that differences in lithology can influence regolith production and material strength. However, both subregions lie within the High Himalaya and are underlain by rock units of broadly similar composition (Dhital, 2015). The optimal cohesion range is also nearly identical in both landscapes, and the success of each parameterisation aligns far more closely with the spatial pattern imposed by its regolith-thickness distribution than with mapped lithological boundaries. Together, these observations indicate that lithology is unlikely to be the primary control on the observed contrasts.

These considerations point instead to an explanation rooted in landscape form. The two subregions differ markedly in relief, degree of dissection, and the extent to which topography promotes either broad elevation control or local convergence (Figure 2). The high-relief, bedrock-dominated terrain of Subregion 1 favours hypsometric control on regolith thickness, whereas the lower-relief, regolith-mantled terrain of Subregion 2 favours curvature-driven local variability. These landscape-scale differences provide a coherent explanation for why certain parameterisations perform well in one subregion but not the other.

4.4 Implications for regolith architecture, curvature dependence, and shallow-failure processes

The differing performance of the regolith-thickness parameterisations demonstrates that topography regulates both the scale and the structure of regolith accumulation, and that this organisation influences coseismic shallow-failure patterns. In Subregion 1, where relief is high and elevation gradients are strong, broad hypsometric trends appear to dominate regolith organisation. Parameterisations that impose systematic thinning of regolith toward higher ridges reproduce the observed failure patterns more effectively than curvature-only formulations. In Subregion 2, where relief is lower, planform convergence is a more important control on regolith distribution, and curvature-informed or hybrid parameterisations yield the closest agreement with the mapped coseismic landslides.

Concave slopes tend to accumulate thicker colluvium, whereas convex slopes are typically regolith-limited. Classical soil-production frameworks link regolith thickness to curvature through non-linear relationships that capture rapid thickening in hollows (Dietrich et al., 1995; Heimsath et al., 1997). In practice, such formulations can be difficult to apply consistently at regional scale because they require piecewise definitions and diverge for negative curvature values. Linear curvature-based parameterisations, such as those explored here, preserve the essential geomorphic meaning of curvature while remaining numerically stable across large and heterogeneous landscapes (Patton et al., 2018). Their strong performance in Subregion 2 reflects the greater abundance of convergent hillslopes and shallow colluvial stores in that landscape (Clubb et al., 2016; Gabet et al., 2021; Hurst et al., 2012). In contrast, curvature alone does not capture the dominant control on regolith thickness in Subregion 1, where regolith distribution is more strongly linked to broad-scale elevation structure, limited colluvial storage, and extensive bedrock exposure.

This behaviour is consistent with findings from other tectonically active mountain belts, including studies in the San Gabriel Mountains, where hillslope form reflects a balance between large-scale relief organisation and local convergence in threshold landscapes (DiBiase et al., 2012). These comparisons reinforce the idea that the scale and style of topographic organisation determine whether hypsometry or curvature exerts the dominant influence on regolith thickness in steep terrain. An important implication of the ensemble is that curvature-based parameterisations should not be assumed to work universally. Curvature performs best in landscapes that follow a ridge-valley template with well-defined convergent hollows (Dietrich et al., 1995; Heimsath et al., 1997). In settings where regolith thickness is controlled primarily by elevation or by patchy bedrock exposure, curvature-only formulations may misrepresent the dominant mode of regolith organisation, underscoring the need for landscape-specific regolith-thickness parameterisations.

These results show that hybrid physical-statistical approaches can be used to test process-based hypotheses about regolith architecture and its influence on coseismic susceptibility. They illustrate how landscape morphology, near-surface material organisation, and strong ground shaking interact to produce regional patterns of shallow failure, while also clarifying the conditions under which deeper, bedrock-dominated failures fall outside the scope of shallow-regolith models.

5 Conclusions

Across two geomorphically contrasting landscapes affected by the 2015 Gorkha earthquake, our results show that regional patterns of coseismic shallow landsliding are governed primarily by the spatial organisation of regolith thickness. Parameterisations that incorporate physically meaningful variability, whether through broad elevation trends, curvature-driven convergence, or both, outperform a uniform-depth baseline and reproduce the distributions of the mapped landslide inventories. A narrow range of moderate effective cohesion ($c' \approx 10$–$15\,\mathrm{kPa}$) yields the closest agreement across all parameterisations and in both subregions. These values are consistent with shallow colluvium and support the conclusion that the failures mobilised near-surface regolith. Cohesion alone, however, cannot explain the contrasting performance of regolith-thickness models across the two landscapes. The high-relief, bedrock-dominated terrain of Subregion 1 is best represented by regolith-thickness distributions that vary primarily with elevation, whereas the lower-relief, regolith-mantled terrain of Subregion 2 requires curvature-informed formulations that capture local planform convergence. These differences align with field-scale characteristics and illustrate how landscape morphology dictates regolith thickness and coseismic landslide response.

Viewed together, the ensemble results demonstrate that physically interpretable regolith-thickness distributions, when coupled with a stability framework that targets population-level correspondence, can reproduce the first-order spatial and statistical structure of coseismic shallow landslide populations. They also show that differences in topographic organisation, rather than uncertainty in failure physics, model resolution, or lithology, explain regional variation in coseismic landslide patterns. These findings provide a scientific basis for understanding how geomorphic processes, regolith architecture, and strong ground shaking interact to produce landscape-scale patterns of coseismic shallow failure.

Software environment and Data availability

ShallowLandslider is implemented in `Python 3.12`, building on the open-source Landlab library (Barnhart et al., 2020; Hobley et al., 2017). Core dependencies include `NumPy`, `Pandas`, `SciPy`, `Matplotlib`, and `scikit-image` for numerical computation and visualization. All model parameters, file paths, and runtime options are defined in a structured `JSON` configuration file, which facilitates repeatable simulations and parameter sweeps. The code for *ShallowLandslider* is undergoing active development, and is freely accessible through its GitHub page: https://github.com/thermok-SG/EQShallowLandslider

Acknowledgements

The authors thank the Community Surface Dynamics Modeling System (CSDMS) for developing and maintaining the Landlab modelling framework used in this study. We also acknowledge OpenTopography for providing access to the DEM data. This research was supported by a NERC Pushing the Frontiers grant to SB (NE/Y000080/1).

Conflict of Interest

The authors declare that there are no conflicts of interest for this manuscript.

References

Avouac, J.-P. P. et al. (2015). "Lower Edge of Locked Main Himalayan Thrust Unzipped by the 2015 Gorkha Earthquake". In: *Nature Geoscience* 8.9, pp. 708–711. DOI: 10.1038/ngeo2518.

Barnhart, K. R. et al. (2020). "Short Communication: Landlab v2.0: A Software Package for Earth Surface Dynamics". In: *Earth Surface Dynamics* 8.2, pp. 379–397. DOI: 10.5194/esurf-8-379-2020.

Campforts, B. et al. (Aug. 2022). "The Art of Landslides: How Stochastic Mass Wasting Shapes Topography and Influences Landscape Dynamics". In: *Journal of Geophysical Research: Earth Surface* 127.8, e2022JF006745. DOI: 10.1029/2022JF006745. (Visited on 01/02/2024).

Catani, F., S. Segoni, and G. Falorni (2010). "An Empirical Geomorphology-Based Approach to the Spatial Prediction of Soil Thickness at Catchment Scale". In: *Water Resources Research* 46.5. DOI: 10.1029/2008WR007450. (Visited on 11/12/2025).

Cho, S. and S. Lee (2002). "Evaluation of Surficial Stability for Homogeneous Slopes Considering Rainfall Characteristics". In: *Journal of Geotechnical and Geoenvironmental Engineering* 128.9, pp. 756–763. DOI: 10.1061/(ASCE)1090-0241(2002)128:9(756).

Clubb, F. J. et al. (2016). "The Relationship between Drainage Density, Erosion Rate, and Hilltop Curvature: Implications for Sediment Transport Processes". In: *Journal of Geophysical Research: Earth Surface* 121.10, pp. 1724–1745. DOI: 10.1002/2015JF003747. (Visited on 12/18/2025).

Dhital, M. R. (2015). "Geology of the Nepal Himalaya: Regional Perspective of the Classic Collided Orogen". In: *Geology of the Nepal Himalaya: Regional Perspective of the Classic Collided Orogen* 1988, pp. 1–498. DOI: 10.1007/978-3-319-02496-7.

DiBiase, R. A., A. M. Heimsath, and K. X. Whipple (June 2012). "Hillslope Response to Tectonic Forcing in Threshold Landscapes". In: *Earth Surface Processes and Landforms* 37.8, pp. 855–865. DOI: 10.1002/esp.3205. (Visited on 02/12/2026).

Dietrich, W. E. et al. (Apr. 1995). "A Process-based Model for Colluvial Soil Depth and Shallow Landsliding Using Digital Elevation Data". In: *Hydrological Processes* 9.3-4, pp. 383–400. DOI: 10.1002/hyp.3360090311. (Visited on 09/04/2025).

Fan, X. et al. (June 2019). "Earthquake-Induced Chains of Geologic Hazards: Patterns, Mechanisms, and Impacts". In: *Reviews of Geophysics* 57.2, pp. 421–503. DOI: 10.1029/2018RG000626. (Visited on 04/25/2024).

Fisher, N. I. (Oct. 1993). *Statistical Analysis of Circular Data*. 1st ed. Cambridge University Press. DOI: 10.1017/CBO9780511564345. (Visited on 10/13/2025).

Gabet, E. J. et al. (2021). “Hilltop Curvature Increases With the Square Root of Erosion Rate”. In: *Journal of Geophysical Research: Earth Surface* 126.5, e2020JF005858. DOI: 10.1029/2020JF005858. (Visited on 12/18/2025).

Gariano, S. L. and F. Guzzetti (Nov. 2016). “Landslides in a Changing Climate”. In: *Earth-Science Reviews* 162, pp. 227–252. DOI: 10.1016/j.earscirev.2016.08.011. (Visited on 11/11/2025).

Harvey, E. L. et al. (Nov. 2024). “Review of Landslide Inventories for Nepal between 2010 and 2021 Reveals Data Gaps in Global Landslide Hotspot”. In: *Natural Hazards*. DOI: 10.1007/s11069-024-07013-1. (Visited on 02/03/2025).

Heimsath, A. M. et al. (July 1997). “The Soil Production Function and Landscape Equilibrium”. In: *Nature* 388.6640, pp. 358–361. DOI: 10.1038/41056. (Visited on 10/02/2024).

Hobley, D. E. et al. (2017). “Creative Computing with Landlab: An Open-Source Toolkit for Building, Coupling, and Exploring Two-Dimensional Numerical Models of Earth-surface Dynamics”. In: *Earth Surface Dynamics* 5.1, pp. 21–46. DOI: 10.5194/esurf-5-21-2017.

Hovius, N. et al. (Apr. 2011). “Prolonged Seismically Induced Erosion and the Mass Balance of a Large Earthquake”. In: *Earth and Planetary Science Letters* 304.3-4, pp. 347–355. DOI: 10.1016/j.epsl.2011.02.005. (Visited on 11/11/2025).

Huang, D. et al. (May 2020). “An Integrated SEM-Newmark Model for Physics-Based Regional Coseismic Landslide Assessment”. In: *Soil Dynamics and Earthquake Engineering* 132, p. 106066. DOI: 10.1016/j.soildyn.2020.106066. (Visited on 05/09/2024).

Hurst, M. D. et al. (2012). “Using Hilltop Curvature to Derive the Spatial Distribution of Erosion Rates”. In: *Journal of Geophysical Research: Earth Surface* 117.F2. DOI: 10.1029/2011JF002057. (Visited on 12/18/2025).

Jibson, R. W., E. L. Harp, and J. A. Michael (Dec. 2000). “A Method for Producing Digital Probabilistic Seismic Landslide Hazard Maps”. In: *Engineering Geology* 58.3-4, pp. 271–289. DOI: 10.1016/S0013-7952(00)00039-9. (Visited on 02/19/2025).

Jibson, R. W. (May 2007). “Regression Models for Estimating Coseismic Landslide Displacement”. In: *Engineering Geology* 91.2-4, pp. 209–218. DOI: 10.1016/j.enggeo.2007.01.013. (Visited on 02/26/2025).

Kargel, J. S. et al. (Dec. 2015). “Geomorphic and Geologic Controls of Geohazards Induced by Nepal’s 2015 Gorkha Earthquake”. In: *Science* 351.6269, aac8353. DOI: 10.1126/science.aac8353. (Visited on 04/23/2025).

Kritikos, T., T. R. Robinson, and T. R. H. Davies (2015). “Regional Coseismic Landslide Hazard Assessment without Historical Landslide Inventories: A New Approach”. In: *Journal of Geophysical Research: Earth Surface* 120.4, pp. 711–729. DOI: 10.1002/2014JF003224. (Visited on 08/13/2025).

Li, A. et al. (Sept. 2017). “Predicting Active-Layer Soil Thickness Using Topographic Variables at a Small Watershed Scale”. In: *PLOS ONE* 12.9, e0183742. DOI: 10.1371/journal.pone.0183742. (Visited on 12/18/2025).

Lombardo, L. et al. (Oct. 2020). “Space-Time Landslide Predictive Modelling”. In: *Earth-Science Reviews* 209, p. 103318. DOI: 10.1016/j.earscirev.2020.103318. (Visited on 12/31/2023).

Meena, S. R. and S. Tavakkoli Piralilou (Oct. 2019). “Comparison of Earthquake-Triggered Landslide Inventories: A Case Study of the 2015 Gorkha Earthquake, Nepal”. In: *Geosciences* 9.10, p. 437. DOI: 10.3390/geosciences9100437. (Visited on 06/04/2025).

Montgomery, D. R. and W. E. Dietrich (Apr. 1994). “A Physically Based Model for the Topographic Control on Shallow Landsliding”. In: *Water Resources Research* 30.4, pp. 1153–1171. DOI: 10.1029/93WR02979. (Visited on 03/12/2024).

Newmark, N. M. (June 1965). “Effects of Earthquakes on Dams and Embankments”. In: *Géotechnique* 15.2, pp. 139–160. DOI: 10.1680/geot.1965.15.2.139. (Visited on 03/19/2025).

Nowicki Jessee, M. A. et al. (2018). “A Global Empirical Model for Near-Real-Time Assessment of Seismically Induced Landslides”. In: *Journal of Geophysical Research: Earth Surface* 123.8, pp. 1835–1859. DOI: 10.1029/2017JF004494. (Visited on 11/06/2025).

Pack, R., D. Tarboton, and C. Goodwin (1998). “The SINMAP Approach to Terrain Stability Mapping”. In: *Proceedings of the 8th Congress of the International Association of Engineering Geology*. Vol. Vol. 2: Engineering Geology and Natural Hazards. Vancouver, Canada.

Park, S. J., K. McSweeney, and B. Lowery (Oct. 2001). “Identification of the Spatial Distribution of Soils Using a Process-Based Terrain Characterization”. In: *Geoderma* 103.3, pp. 249–272. DOI: 10.1016/S0016-7061(01)00042-8. (Visited on 11/12/2025).

Parker, R. N. et al. (Oct. 2015). “Spatial Distributions of Earthquake-Induced Landslides and Hillslope Preconditioning in the Northwest South Island, New Zealand”. In: *Earth Surface Dynamics* 3.4, pp. 501–525. DOI: 10.5194/esurf-3-501-2015. (Visited on 08/13/2025).

Parker, R. N. et al. (Sept. 2016). “Colluvium Supply in Humid Regions Limits the Frequency of Storm-Triggered Landslides”. In: *Scientific Reports* 6.1, p. 34438. DOI: 10.1038/srep34438. (Visited on 03/12/2024).

Patton, N. R. et al. (Aug. 2018). “Predicting Soil Thickness on Soil Mantled Hillslopes”. In: *Nature Communications* 9.1, p. 3329. DOI: 10.1038/s41467-018-05743-y. (Visited on 07/10/2024).

Pelletier, J. D. and C. Rasmussen (2009). “Geomorphically Based Predictive Mapping of Soil Thickness in Upland Watersheds”. In: *Water Resources Research* 45.9. DOI: 10.1029/2008WR007319. (Visited on 08/13/2025).

Petley, D. (Oct. 2012). “Global Patterns of Loss of Life from Landslides”. In: *Geology* 40.10, pp. 927–930. DOI: 10.1130/G33217.1. (Visited on 11/11/2025).

Reichenbach, P. et al. (May 2018). “A Review of Statistically-Based Landslide Susceptibility Models”. In: *Earth-Science Reviews* 180, pp. 60–91. DOI: 10.1016/j.earscirev.2018.03.001. (Visited on 08/13/2025).

Roback, K. et al. (2017). *Map Data of Landslides Triggered by the 25 April 2015 Mw 7.8 Gorkha, Nepal Earthquake: ,* DOI: 10.5066/F7DZ06F9.

— (2018). "The Size, Distribution, and Mobility of Landslides Caused by the 2015 Mw7.8 Gorkha Earthquake, Nepal". In: *Geomorphology* 301, pp. 121–138. DOI: 10.1016/j.geomorph.2017.01.030.

Romeo, R. (Dec. 2000). "Seismically Induced Landslide Displacements: A Predictive Model". In: *Engineering Geology* 58.3, pp. 337–351. DOI: 10.1016/S0013-7952(00)00042-9. (Visited on 04/23/2024).

Rubner, Y., C. Tomasi, and L. J. Guibas (Nov. 2000). "The Earth Mover's Distance as a Metric for Image Retrieval". In: *International Journal of Computer Vision* 40.2, pp. 99–121. DOI: 10.1023/A:1026543900054. (Visited on 10/13/2025).

Segoni, S., G. Rossi, and F. Catani (Mar. 2012). "Improving Basin Scale Shallow Landslide Modelling Using Reliable Soil Thickness Maps". In: *Natural Hazards* 61.1, pp. 85–101. DOI: 10.1007/s11069-011-9770-3. (Visited on 11/03/2025).

Tanyaş, H. et al. (2017). "Presentation and Analysis of a Worldwide Database of Earthquake-Induced Landslide Inventories". In: *Journal of Geophysical Research: Earth Surface* 122.10, pp. 1991–2015. DOI: 10.1002/2017JF004236. (Visited on 03/27/2025).

USGS (2015). *M 7.8 - 67 Km NNE of Bharatpur, Nepal.* https://earthquake.usgs.gov/earthquakes/eventpage/us20002926. (Visited on 11/05/2015).

Wang, J. et al. (June 2020). "Long-Term Patterns of Hillslope Erosion by Earthquake-Induced Landslides Shape Mountain Landscapes". In: *Science Advances* 6.23, eaaz6446. DOI: 10.1126/sciadv.aaz6446. (Visited on 11/06/2025).

Wong, H. and K. Ho (2000). *Preliminary Quantitative Risk Assessment of Earthquake-Induced Landslides at Man-Made Slopes in Hong Kong.* Tech. rep. GEO Report No. 98. Hong Kong SAR: Civil Engineering Department: Geotechnical Engineering Office.

Zevenbergen, L. W. and C. R. Thorne (Jan. 1987). "Quantitative Analysis of Land Surface Topography". In: *Earth Surface Processes and Landforms* 12.1, pp. 47–56. DOI: 10.1002/esp.3290120107. (Visited on 09/04/2025).